USGS

Hayward Fault Rocks: Porosity, Density and Strength Measurements

by C.A. Morrow and D.A. Lockner[1]

Open-File Report 01–421

2001

U.S. DEPARTMENT OF THE INTERIOR
U.S. GEOLOGICAL SURVEY

[1]Menlo Park, Calif.

Abstract

Porosity, density and strength measurements were conducted on rock samples collected from the Hayward Fault region in Northern California as part of the Hayward Fault Working Group's efforts to create a working model of the Hayward Fault. The rocks included in this study were both fine and coarse grained gabbros, altered keratophyre, basalt, sandstone, and serpentinite from various rock formations adjacent to the Hayward Fault.

Densities ranged from a low of 2.25 gm/cc (altered keratophyre) to 3.05 gm/cc (fine gabbro), with an average of 2.6 gm/cc, typical of many other rocks. Porosities were generally around 1% or less, with the exception of the sandstone (7.6%) and altered keratophyre (13.5%).

Failure and frictional sliding tests were conducted on intact rock cylinders at room temperature under effective pressure conditions of up to 192 MPa, simulating depths of burial to 12 km. Axial shortening of the samples progressed at a rate of 0.1 μm/sec (fine samples) or 0.2 μm/sec (porous samples) for 6 mm of displacement. Velocity stepping tests were then conducted for an additional 2 mm of displacement, for a total of 8 mm. Both peak strength (usually failure strength) and frictional strength, determined at 8 mm of displacement, increased systematically with effective pressure. Coefficients of friction, based on the observed fracture angles, ranged from 0.6 to 0.85, consistent with Byerlee's Law. Possible secondary influences on the strength of the Hayward rock samples may be surface weathering, or a larger number of pre-existing fractures due to the proximity to the Hayward Fault. All samples showed velocity strengthening, so that the average a-b values were all strongly positive. There was no systematic relation between a-b values and effective pressure. Velocity strengthening behavior is associated with stable sliding (creep), as observed in the shallow portions of the Hayward Fault.

Introduction

The Hayward Fault Working Group is undertaking a collaborative effort of field and laboratory investigations to better understand the complexities of the Hayward Fault Zone and its potential to generate large earthquakes. The project combines laboratory studies of rock strength, rock magnetism, and seismic velocity with detailed geologic, aeromagnetic and seismic field studies in order to create a 3-D model of the fault behavior. This project has particular significance because the Hayward Fault is cited as the most probable source of a large earthquake in the San Francisco Bay Area within the next 30 years (*Working Group on California Earthquake Probabilities*, 1999). This fault generated a M6.9 earthquake in 1868, with a surface rupture approximately 40 km long.

Considerable work has focused on locating and mapping various segments of the fault system, and to determine the paleotectonics of the region (e.g., *Herd*, 1978; *Lienkaemper*, 1992; *Graymer et al.*, 1995). *Graymer et al.* (2001) show that the western Hayward Fault has about 100 km total right-lateral offset with a sporadic history of movement, and that the active fault zone encompasses a number of strands in a zone up to 1 km wide, based on the reconstruction of offset geologic formations in the area, measured creep rates and other field evidence. Because the Hayward Fault Zone includes many different rock formations, it is necessary to study a variety of samples in order to characterize the materials properties in the fault zone. In this study, we have determined the failure and frictional strength, density and porosity of representative rocks available in outcrops from a number of formations adjacent to the fault. Results show that rock strengths are tied to rock type as expected, frictional strengths generally follow Byerlee's Law, (*Byerlee*, 1978), with a coefficient of friction between 0.6 and 0.85, and all rocks show velocity-strengthening behavior.

Sample Description

Samples were collected from surface outcrops of several rock formations near the Hayward Fault by Russell Graymer in the summer of 1998. They include a coarse and fine-grained gabbro, an altered and unaltered keratophyre, basalt and sandstone. Serpentinite samples were too friable to be successfully cored. Because the serpentinites are an important rock type along the Hayward Fault, and the focus of the aeromagnetic studies, we have substituted a similar antigorite-rich specimen from New Idria, California, described by *Moore et al.*, (1997). *Moore and Ponce*, (2001) discuss the petrography and magnetic properties of the samples used in this study. Measurements of seismic velocity (unpublished) were also made on the same samples. Brief petrologic descriptions are included below:

Fine-grained gabbro (sample #101)

This rock contains mostly equal portions of euhedral plagioclase and amphibole crystals roughly 0.05-0.85 mm in diameter, with lesser magnetite and other minor minerals. Small cracks in various orientations are filled with secondary chlorite, titanite and calcite. The rock appears fresh with little evidence of weathering.

Altered Keratophyre (sample #102)

This keratophyre has been heavily altered to a fine-grained, quartz-rich rock in which the original granular texture is lost. Numerous small veins of quartz are present, as well as Fe- and Ti-oxide bands bordered by an Si-Al bearing mineral, probably kaolinite. Small cracks and voids (up to 1 cm long) occur in every orientation, however the bulk rock contains larger flaws that were avoided during coring.

Coarse-grained gabbro (sample #103)

This rock contains 50 % plagioclase and nearly equal portions (12%) of clinopyroxene and orthopyroxene, with minor zeolite, amphibole, phyllosilicate, and other phases. Grains are 2-3 mm long. Subparallel veins are filled with prehnite and thomsonite. There is minimal evidence of weathering.

Basalt (sample #107)

This is a coarse-grained, vesicular basalt with 28% plagioclase phenocrysts set in a matrix of originally mafic minerals that have since altered to calcite (41%) and chlorite (18%). Minor quartz, opaques and titanite are present. Veins and fractures are calcite-filled, and some contain weathering features along the crack walls. Fractures have no preferred orientation.

Keratophyre (sample #111)

This rock contains irregular quartz and feldspar phenocrysts, along with lithic fragments, in a fine-grained quartzofeldspathic groundmass. Narrow cracks with no preferred orientation are present. Weathering is evident through various sections of the rock.

Joaquin Miller Sandstone (sample #114)

The Joaquin Miller is a cretaceous graywacke consisting of lithic fragments (34%), single crystal clasts of mostly quartz and feldspars (52%) and matrix material (14%), including calcite, chlorite, Fe-oxides and other lesser constituents. There is no evidence of bedding, intergranular cracking, or weathering.

New Idria Serpentinite (NI)

This rock is composed of 76% serpentine, mostly antigorite, with numerous veins of calcite and chrysotile. Serpentinites collected from the Hayward Fault area were also antigorite rich.

Procedure

Density and Porosity

Cylindrical core samples were prepared from the field specimens. In general, core samples were taken from the more intact areas of the rock, avoiding the major fractures that make coring difficult. This introduces a bias in the sampling, so that our porosity and density measurements represent the matrix rock rather than bulk rock formation. The cored samples, 2.54 cm in both diameter and length, were vacuum-dried overnight in an oven to remove residual water. They were then weighed to determine dry weight, W_d, and density (Table 1). For the porosity calculations, the samples were fully saturated in the vacuum oven and weighed while suspended in water to determine wet weight, W_w. Porosity, Φ, is defined as

$$\Phi = 1\text{-}[(W_d - W_w)/ \text{Sample Volume}] \quad (1)$$

Strength

Room temperature triaxial strength tests were performed in the laboratory on intact cylindrical samples 2.54 cm in diameter and 6.35 cm long. Some samples were shorter if the available rock was insufficient. The core samples were pre-saturated in a vacuum oven to remove air. They were then jacketed in polyurethane and secured between two steel endplugs with hose clamps. A stainless steal mesh between the top of the sample and the top end plug assured that water could penetrate the sample evenly. The sample assembly was placed in a pressure vessel and air was evacuated from the sample system. Confining

and pore pressure was applied to the samples for effective pressures of 32, 64, 128, and 192 MPa, simulating depths of burial of 2, 4, 8, and 12 km respectively. Only one core of the keratophyre (sample 111) was available. This sample was tested at the lowest effective pressure of 32 MPa (simulating 2 km depth). Pressure values were determined assuming an average sample density of 2.6 gm/cc, and are listed in Table 2. An axial load was applied to the samples at a rate of either 0.1 μm/sec or 0.2 μm/sec for 6 mm of displacement (Table 3) during which time the samples failed and then continued to slide on the newly formed shear fracture. The deformation rate depended on the porosity of the samples in order to ensure that pore pressure equilibrated as the samples deformed, and that the samples remained fully saturated throughout the experiments. During sliding from 6 to 8 mm, the axial shortening rate alternated in factor-of-ten steps; first ten times faster at 6.0 mm, then back to the original rate at 7 mm, ten times slower at 7.3 mm, and finally back to the original rate at 7.5 mm (Table 3). Small variations in strength during the rate steps allow us to determine the velocity dependence of frictional strength.

Results

Density and Porosity

Most samples have densities that fall in a range typical of their rock type and grain size, with an average of around 2.6. The altered keratophyre had such visible sample variability that two cores were tested and the numbers averaged. This rock had the lowest density, at 2.25 gms/cc. At the other extreme was the fine-grained gabbro, with a density of 3.05 gms/cc. Measured porosities follow the trend of density in most cases. Values ranged from 0.2% (fine-grained gabbro) to 13.5% (altered keratophyre). Many samples have porosities around 1-5%, typical of fine-grained intact rocks. The porosities reported

here should be considered minimum values. These measurements are consistent with density measurements made on similar Hayward Fault rocks by Moore and Ponce (2001).

Strength

Differential stress (measured load minus confining pressure) versus axial displacement is shown in Figure 1 for all samples. The strength of the samples was a function of effective pressure as expected. The strength behavior during shearing fell into three categories: Many samples failed during the first few mm of displacement with a dynamic stress drop, often characterized by a total stress drop (gabbro, keratophyre, serpentine). The coarse gabbro, basalt, and sandstone failed slowly (quasi-statically), with a more gradual stress drop after peak strength was achieved. The altered keratophyre gradually reached peak strength and slid stably thereafter, so that the failure and sliding strengths were the same. All samples developed through-going faults.

Peak strength versus effective pressure is shown for all samples in Figure 2. (See also Table 4 for a complete tabulation of strength results). Strength correlated well with density and porosity, systematically increasing from the weak, altered keratophyre to the stronger gabbros and basalt. Differential stress after failure, or "frictional strength", measured at 8 mm of sliding (Figure 3), also increased systematically with effective pressure. These values were more similar between rock types than the peak (failure) strength shown in the previous figure. The trend of the data for the two gabbros and basalt increased uncharacteristically at the highest pressure of 192 MPa. One possible interpretation may be that these samples were not fully saturated once shearing commenced because of rock dilation, and so the effective pressure may have been higher than suspected inside the rock. This possibility is the reason why the denser samples were run at the slower rates.

Samples fractured at angles ranging from 20 to 47° from vertical, most around 30-32° (Table 4). In some cases the angle was controlled by the orientation of pre-existing

fractures, both fresh or healed with secondary minerals. Also, some samples failed with multiple fractures or in a barrel-shaped manner. The principal fracture angle was recorded for these rocks. Effective coefficients of friction were determined from the fracture angles and recorded stresses of each sample according to the following relations:

$$P_{diff} = \text{axial load} - P_c \quad (2)$$

$$\theta = \text{fracture angle} \quad (3)$$

$$\sigma_s = (P_{diff}/2)(\sin(2\theta)) \quad (4)$$

$$\sigma_{n,\,eff} = (Pc + (P_{diff}/2)(1-\cos(2\theta))) - P_p \quad (5)$$

$$\mu_{eff} = \sigma_s/\sigma_{n,\,eff} \quad (6)$$

where P_{diff} is differential pressure, P_c is confining pressure, σ_s is shear stress, $\sigma_{n,\,eff}$ is effective normal stress, P_p is pore pressure, and μ_{eff} is the effective coefficient of friction. Effective coefficient of friction (Equation 6.) versus axial displacement is shown for all samples in Figure 4. Although the shapes of these curves are similar to the differential stress plots, the trends with pressure are not necessarily the same. Note that in general, the displacements at which peak strength is reached are directly proportional to effective pressure. The sliding portions of the curves are less systematic. Many friction values at failure are above 1.0 (gabbros, basalt, keratophyre, and sandstone). Post-failure, as the samples slid on newly formed fractures, the coefficients of friction were generally between 0.6 and 0.85, in agreement with Byerlee's Law (*Byerlee*, 1978), although at some pressures, the gabbros and basalt exceed these values. Once again the weak altered keratophyre was the exception, with coefficients of friction from 0.45 to 0.57.

Coefficients of friction for all the samples (at 8 mm displacement) are summarized in Figure 5, showing no dependence on effective pressure.

Because of the large range in failure angles, it is of interest to determine whether this variable is responsible for the differences in strengths. Many frictional sliding experiments are conducted on samples containing a pre-existing sawcut, usually 30-35° from vertical. Taking 30° as a standard, we computed failure and frictional sliding coefficients of friction (Table 4) for comparison. Results show varying differences in the peak strength, but the effect on frictional strength is insignificant, as seen in the example in Figure 6 (keratophyre 111).

Velocity Dependence

All samples showed velocity strengthening, that is, the coefficient of friction increased when the rate of displacement increased, as shown by the steps in the friction curves at 6 and 7.5 mm of sliding (Figure 4). When the velocity decreased by an order of magnitude at 7.0 and 7.3 mm, the samples became slightly weaker. Because these steps are often hard to see at the scale plotted in Figure 4, a blowup of one of the more easy-to-interpret samples (altered keratophyre) is shown in Figure 7. The frictional resistance of the rock changes abruptly when the loading rate changes and can easily be read off the plot. For some samples, this change is more gradual, so that a certain amount of displacement is required before the final friction value can be read.

The velocity dependence of friction is described by two constitutive parameters, a, the direct initial response, defined as

$$a = \Delta\mu/\ln(V_1/V_2), \tag{7}$$

and b, the magnitude of the decay to a steady-state value, defined by

$$a\text{-}b = \Delta\mu^{ss}/\ln(V_1/V_2), \tag{8}$$

where $\Delta\mu$ is the change in the coefficient of friction, μ^{ss} is the steady-state coefficient of friction and V_1 and V_2 are the sliding velocities before and after the change of rate, respectively (*Logan and Rauenzahn*, 1987). Velocity dependence can be negative, that is, samples can become slightly weaker at faster sliding velocities. Although our tests were all conducted at room temperature, velocity effects are known to be temperature dependent, particularly for water-saturated samples (e.g., *Blanpied et al.*, 1995). Most importantly, velocity effects are linked to fault stability, where positive values correspond to stable fault sliding and negative values are associated with unstable slip.

The average a-b values for each of the samples (Figure 8 and Table 4) are not systematically related to effective pressure, although all values are positive. Also, the general range of a-b values does not appear to depend on rock type, density, or porosity. For instance, both the sandstone and altered keratophyre, the most porous samples, have similar a-b values of around 0.005, but the coarse gabbro is also within this range. Both the finer gabbro and basalt samples have high a-b values of around 0.01 at an effective pressure of 128 MPa, but at other pressures the a-b values are again around 0.005. Only the serpentine shows a consistent trend of high velocity dependence, reaching a value of 0.015 at 128 MPa effective pressure.

It is possible that the velocity dependence of the Hayward rocks may be affected to some degree by the abundant alteration products that line the cracks and pores of the samples, described in *Moore and Ponce,* (2001). Often, failure occurred along pre-existing fractures that were lined or completely healed with secondary minerals such as zeolites, chlorite or calcite. The velocity dependence of strength for many alteration minerals is unknown at this time, so the overall effect on rock strength, if any, is unclear.

Discussion

There are several factors that may affect the strength of the Hayward samples. Many of the samples contained macroscopic fractures, both healed and unhealed, that could serve as planes of weakness when loaded. Indeed, some of the samples failed along these fractures. Other samples, such as the gabbros, contained narrow cracks observed in thin section, often filled with secondary minerals. These small cracks may also be nucleation points for failure. In addition, the rocks were collected from surface outcrops where they were subjected to weathering, and it is possible that some samples may not be representative of the equivalent rocks at depth. *Moore and Ponce* (2001) describe the extent of the weathering in these rocks, which they found to be minimal in most samples. However, some weathering features were observed along microcrack walls, and thus may also have an influence on overall sample strength. With these points in mind, we none-the-less observe that the frictional strengths of the samples were generally within the range of Byerlee's Law. Thus, our suite of Hayward Fault rocks had "typical" frictional strengths that were appropriate to their rock type.

What do these results tell us about the Hayward Fault? Our study shows that there is a range of rock strengths among the coherent outcrops that we sampled in the fault zone, reflecting the variety of rock formations in the area. There were no rocks with coefficients of friction less than 0.4 (as might be observed with a layer of saturated, clay-rich fault gouge), which would be of particular interest when modeling the behavior of the Hayward Fault. However, it is possible that there may be regions where small contrasts in rock strength may influence the overall rheological properties of adjacent rock formations, such as where a serpentinite body abuts a slightly stronger basalt or gabbro formation. Of note is that all of the rocks displayed velocity strengthening, that is, they were stronger at the faster sliding rates. This effect is quantified by their a-b values, which were all positive, ranging from 0.003 to 0.015. Positive a-b values are associated with stable sliding (creep),

and indeed the shallow portion of the Hayward Fault is observed to creep. This result is an important facet of the Hayward Fault Working Group's 3-D model of the Hayward Fault.

References

Blanpied, M.L., Lockner, D.A., and Byerlee, J.D., 1995, Frictional slip of granite at hydrothermal conditions, *J. Geophy. Res*., *100*, B7, 13045-13064.

Byerlee, J.D., 1978, The friction of rocks, *Pure Apply. Geophy*., *116*, 615-626.

Graymer, R.W., Jones, D.L., and Brabb, E.E., 1995, Geologic map of the Hayward Fault Zone, Contra Costa, Alameda and Santa Clara Counties, California: A digital database, *U.S. Geol. Surv. Open-file Report 95-597*.

Graymer, R.W., Sarna-Wojciki, A.M., Walter, J.P., and McLaughlin, R.J., 2001, Controls on timing and amount of right-lateral offset on the East Bay Fault System, San Francisco Bay region, California, in review.

Herd, D.G., 1978, Map of Quaternary faulting along the northern Hayward Fault Zone, *U.S. Geol. Surv. Open-file Report 78-308*, scale 124,000.

Lienkaemper, J.J., 1992, Map of recently active traces of the Hayward fault, Alameda and Contra Costa Counties, California, *U.S. Geol. Surv. Misc. Field Studies Map MF-2196*, 13pp., scale 1:24,000.

Logan, J.M., and Rauenzahn, K.A., 1987, Frictional dependence of gouge mixtures of quartz and montmorillonite on velocity, composition and fabric, *Tectonophy.*, *144*, 87-108.

Moore, D.E., Lockner, D.A., Shengli, M., Summers, R, and Byerlee, J.D., 1997, Strengths of serpentinite gouges at elevated temperatures, *J. Geophy. Res.*, *102*, 14787-14801.

Moore, D.E., and Ponce D.A., 2001, Petrography and physical properties of selected rock types associated with the Hayward Fault, *U.S.G.S. Open-File Report 01-263*.

Working Group on California Earthquake Probabilities, Earthquake probabilities in the San Francisco Bay Region: 2000 to 2030 – A summary of findings, 1999, *U.S. Geol. Surv. Open-File Report* 99-517.

Table 1. Hayward Fault Rock Density and Porosity

Sample	Description	Volume	dry wt.	Density	wet wt.	ϕ
98R-101-9	fine grained gabbro	12.870 cc	39.0935	3.0589	26.2515	0.0022
98R-102-8	keratophyre (altered)	12.870	28.2914	2.2137	17.5020	0.1616
98R-102-9		11.274	25.8056	2.2889	15.7575	0.1087
				2.2513av.		0.1351av.
98R-103-8	coarse gr. gabbro	12.870	36.5498	2.8599	23.8389	0.0123
98R-107-6	basalt	12.870	34.7474	2.7188	21.9441	0.0052
98R-111-3	keratophyre	12.900	32.3030	2.5041	19.8733	0.0364
98R-114-7	sandstone	12.870	31.5480	2.4685	19.6679	0.0769
New Idria-8	Serpentinite	12.870	32.4145	2.3635	19.8766	0.0258

porosity, $\phi = 1 - [(\text{dry wt.} - \text{wet wt.})/ \text{volume}]$

density = dry wt./volume

wet wt.= weight while suspended in water

Table 2. Simulated Depths and Corresponding Experimental Pressures

Depth (km)	P_p (MPa)*	P_c (MPa)†	P_e (MPa)
2	20	52	32
4	40	104	64
8	80	208	128
12	120	312	192

* P_p (pore pressure) = 0.01 MPa/ meter
† P_c (confining pressure) = 2.6 P_p
P_e (effective pressure) = P_c - P_p

Table 3. Velocity Stepping Schedule

Displacement (mm)	Rate (μm/sec)*	Rate (μm/sec)†
0.0 – 6.0	0.1	0.2
6.0 – 7.0	1.0	2.0
7.0 - 7.3	0.1	0.2
7.3 – 7.5	0.01	0.02
7.5 – 8.0	0.1	0.2

*Displacement rate for denser samples:
- Fine Gabbro
- Coarse Gabbro
- Basalt
- Keratophyre
- Serpentine

† Displacement rate for porous samples:
- Altered Keratophyre
- Sandstone

Table 4. Hayward Fault Sample Results

Sample	run #	P_e (MPa)	failure angle (°)	failure streng. (MPa)	failure μ observed	failure μ at 30°	sliding strength (MPa)	sliding μ observed	sliding μ at 30°	a-b
gabbro 101-1	hay4	32	47	264.2	0.760	1.17	121.9	0.62	0.840	0.00390
gabbro 101-2	hay9	64	30	481.7	1.13	1.13	188.4	0.73	0.730	0.00560
gabbro 101-6	hay26	128	33	583.1	0.880	0.920	352.2	0.69	0.700	0.0115
gabbro 101-3	hay25	192	30	794.3	0.880	0.880	716.5	0.83	0.830	0.00380
altrd kerat 102-1	hay2	32	32	79.90	0.660	0.660	63.40	0.57	0.570	0.00500
altrd kerat 102-2	hay13	64	37	111.2	0.510	0.520	111.2	0.51	0.520	0.00360
altrd kerat 102-3	hay15	128	34	238.1	0.540	0.550	215.3	0.51	0.510	0.00380
altrd kerat 102-5	hay21	192	45	291.7	0.430	0.470	159.5	0.45	0.510	0.00390
crs. gabbro 103-1	hay3	32	30	241.0	1.13	1.13	56.20	0.87	0.870	0.00630
crs. gabbro 103-2	hay10	64	30	341.4	0.990	0.990	170.5	0.69	0.690	0.00790
crs. gabbro 103-3	hay17	128	32	613.6	0.920	0.940	341.1	0.68	0.690	0.00450
crs. gabbro 103-4	hay 22	192	35	775.4	0.810	0.870	673.2	0.76	0.810	0.00510
basalt 107-1	hay6	32	30	222.4	1.10	1.10	94.30	0.73	0.730	0.00620
basalt 107-2	hay11	64	32	399.6	1.02	1.05	261.7	0.85	0.870	0.00580
basalt 107-3	hay18	128	31	561.6	0.890	0.900	291.6	0.63	0.630	0.00980
basalt 107-4	hay23	192	33	759.5	0.830	0.860	644.6	0.77	0.790	0.00450
keratophyre 111-1	hay7	32	20	303.9	1.44	1.22	126.4	0.87	0.860	0.00530
sandstone 114A-1	hay5	32	27	206.5	1.12	1.06	83.10	0.68	0.680	0.00610
sandstone 114A-2	hay14	64	32	345.1	0.960	0.990	150.1	0.63	0.640	0.00470
sandstone 114A-3	hay16	128	34	490.0	0.810	0.840	293.0	0.62	0.630	0.00480
sandstone 114A-4	hay20	192	33	517.9	0.680	0.690	370.7	0.56	0.560	0.00470
serpentinite NI-1	hay8	32	31	141.8	0.900	0.910	58.50	0.54	0.540	0.00670
serpentinite NI-5	hay12	64	32	312.6	0.920	0.950	165.6	0.67	0.680	0.0153
serpentinite NI-3	hay19	128	32	348.5	0.690	0.700	242.7	0.56	0.560	0.0114
serpentinite NI-2	hay24	192	37	434.4	0.600	0.620	305.3	0.48	0.490	0.0101

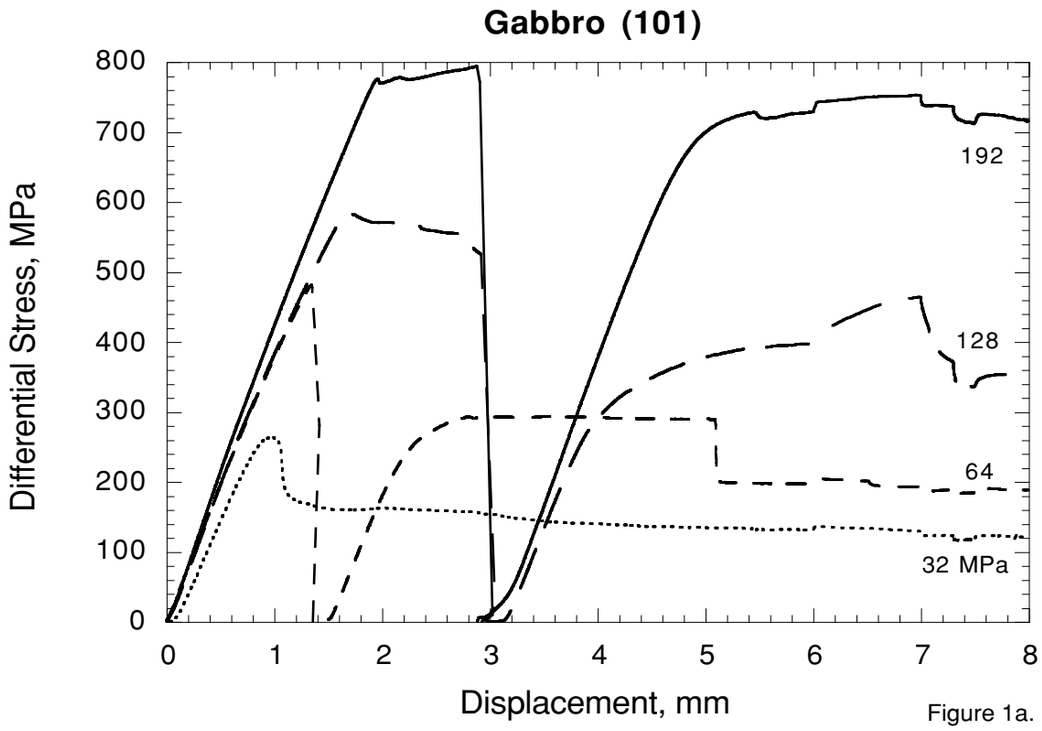

Figure 1a.

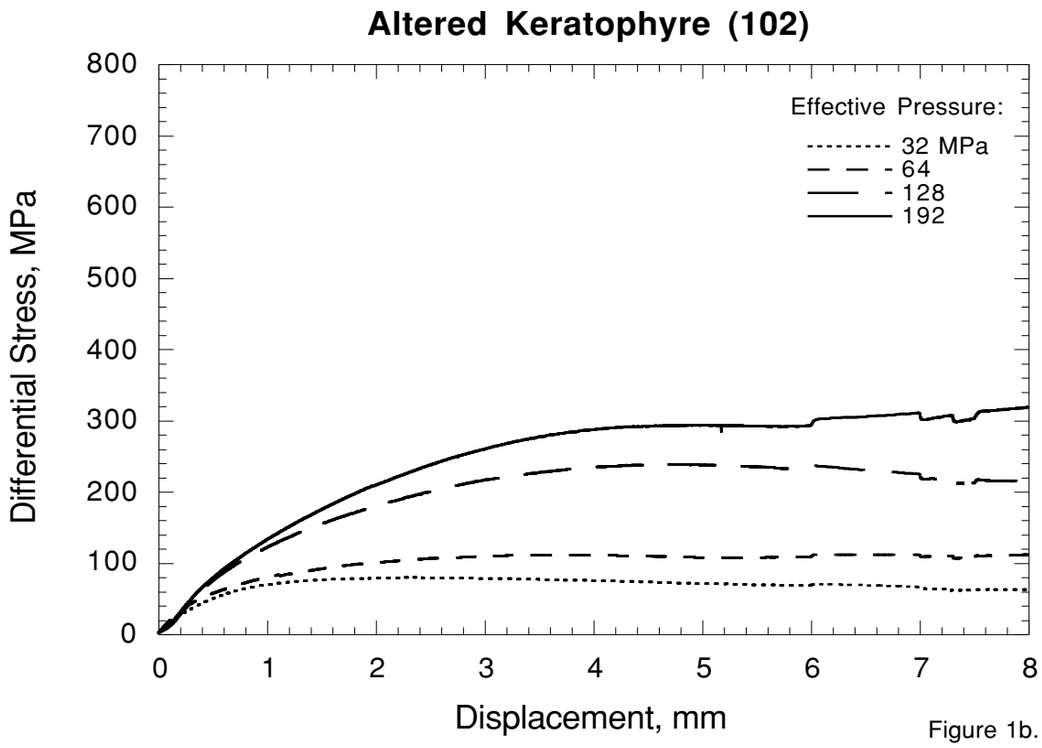

Figure 1b.

Figure 1. Differential stress (axial load - confining pressure) versus displacement at effective pressures of 32, 64, 128, and 192 MPa, representing depths of burial of 2, 4, 8, and 12 km. a., Gabbro (101); b., Altered Keratophyre (102); c., Coarse Gabbro (103); d., Basalt (107); e., Keratophyre (111); f., Sandstone (114); and g., Serpentine (New Idria).

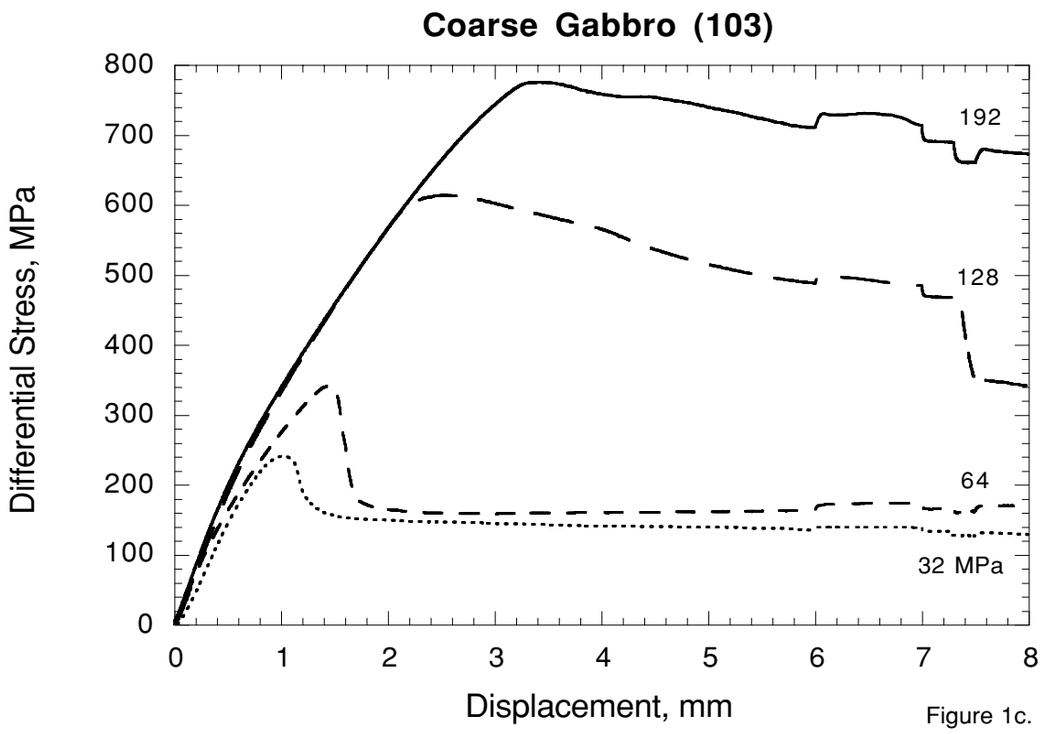

Figure 1c.

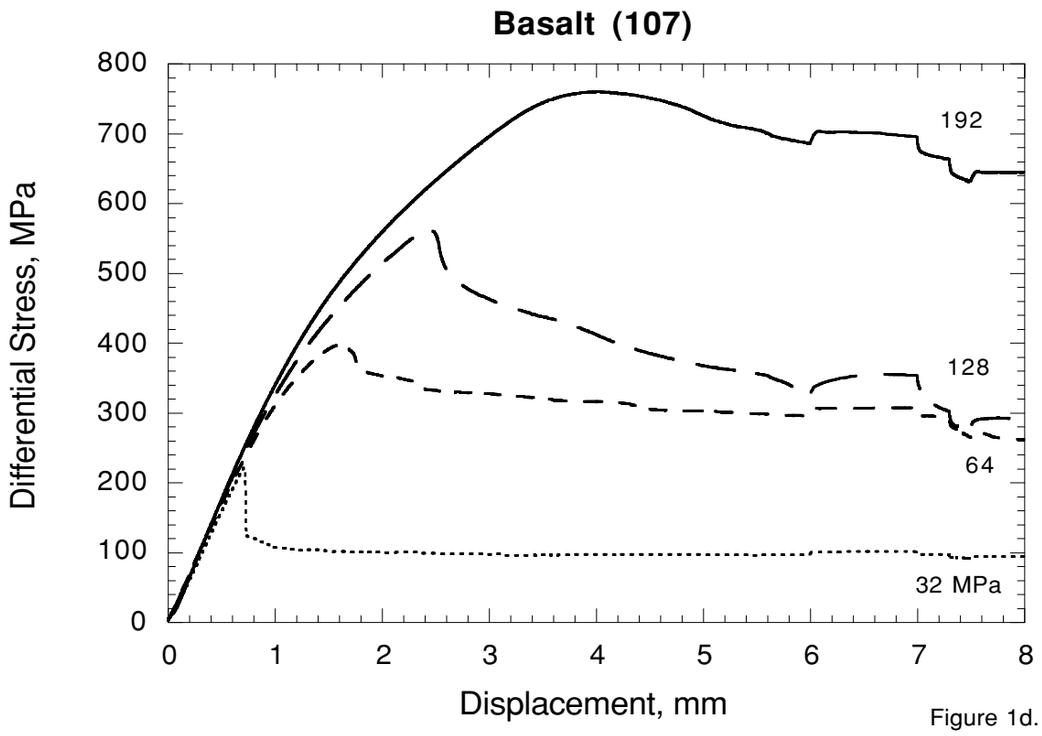

Figure 1d.

Figure 1. Differential stress (axial load - confining pressure) versus displacement at effective pressures of 32, 64, 128, and 192 MPa, representing depths of burial of 2, 4, 8, and 12 km. a., Gabbro (101); b., Altered Keratophyre (102); c., Coarse Gabbro (103); d., Basalt (107); e., Keratophyre (111); f., Sandstone (114); and g., Serpentine (New Idria).

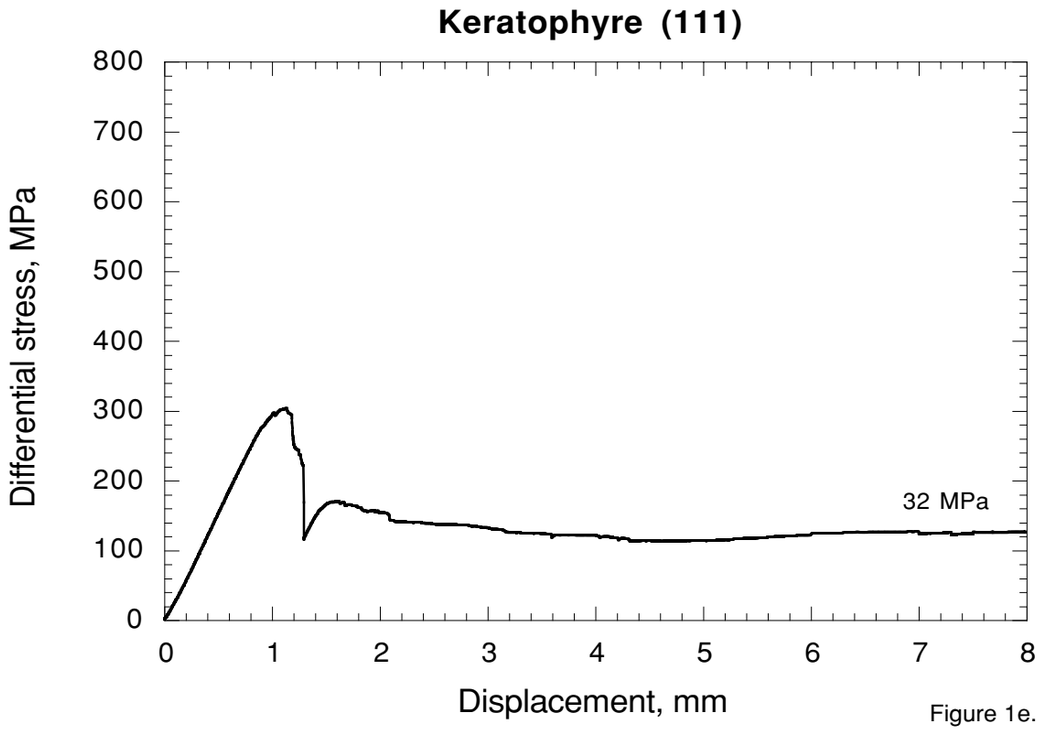

Figure 1e.

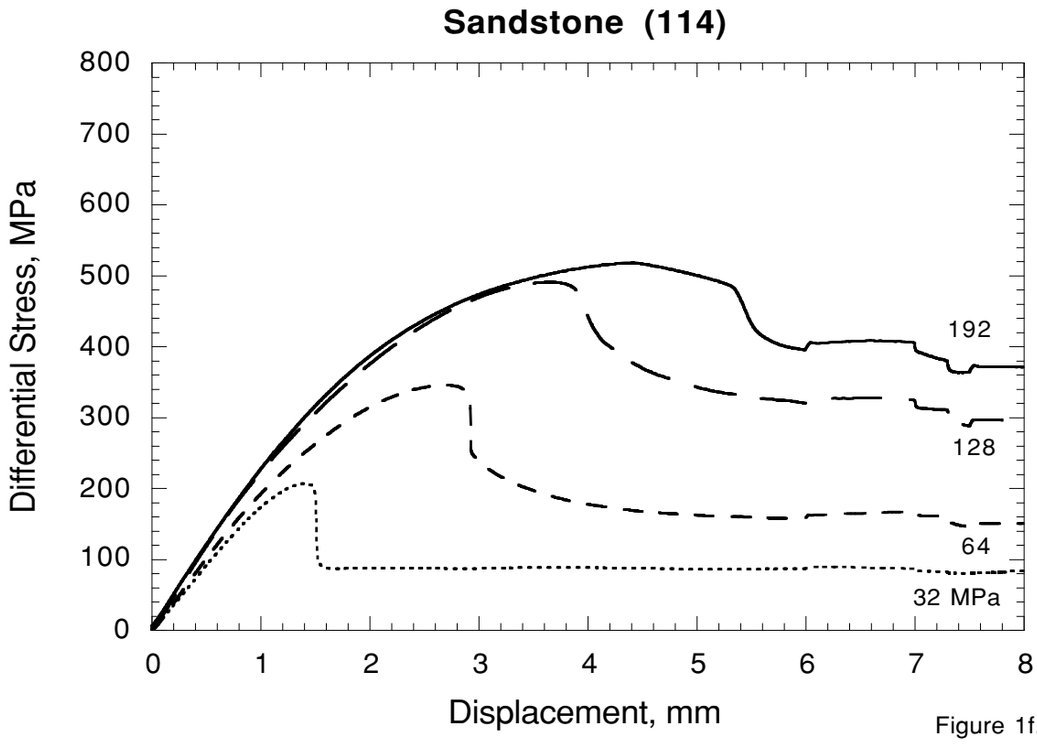

Figure 1f.

Figure 1. Differential stress (axial load - confining pressure) versus displacement at effective pressures of 32, 64, 128, and 192 MPa, representing depths of burial of 2, 4, 8, and 12 km. a., Gabbro (101); b., Altered Keratophyre (102); c., Coarse Gabbro (103); d., Basalt (107); e., Keratophyre (111); f., Sandstone (114); and g., Serpentine (New Idria).

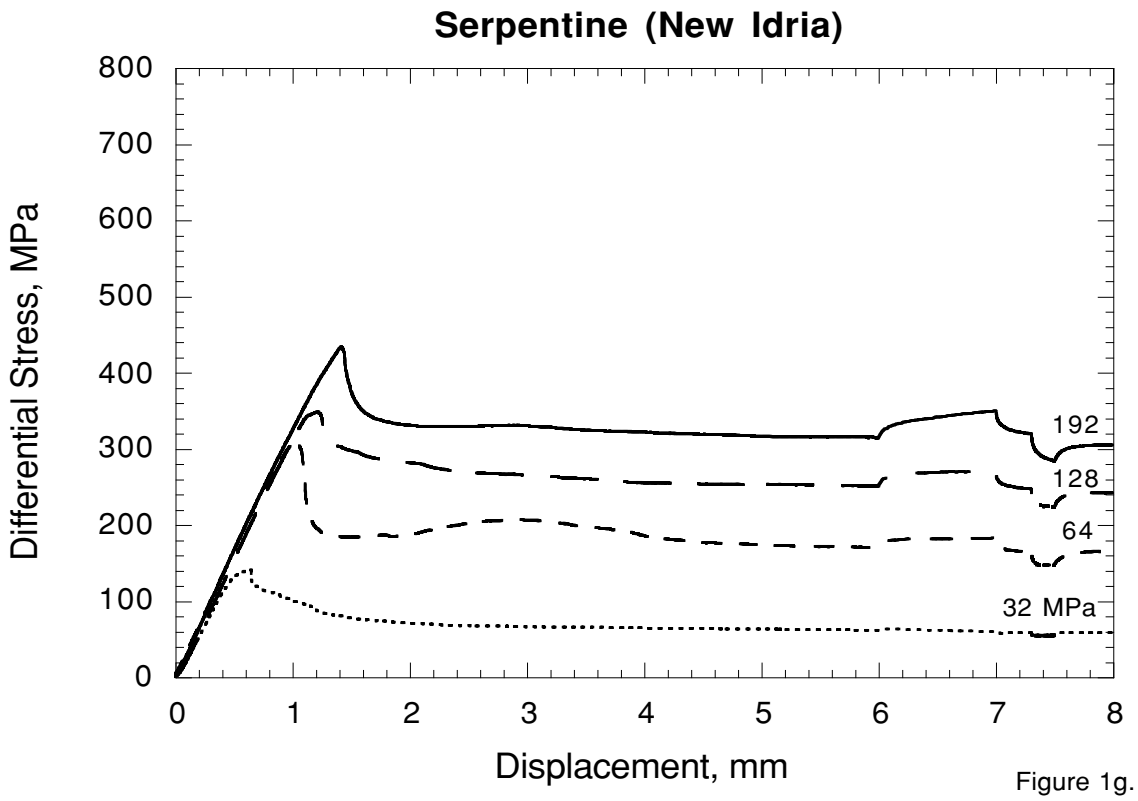

Figure 1. Differential stress (axial load - confining pressure) versus displacement at effective pressures of 32, 64, 128, and 192 MPa, representing depths of burial of 2, 4, 8, and 12 km. a., Gabbro (101); b., Altered Keratophyre (102); c., Coarse Gabbro (103); d., Basalt (107); e., Keratophyre (111); f., Sandstone (114); and g., Serpentine (New Idria).

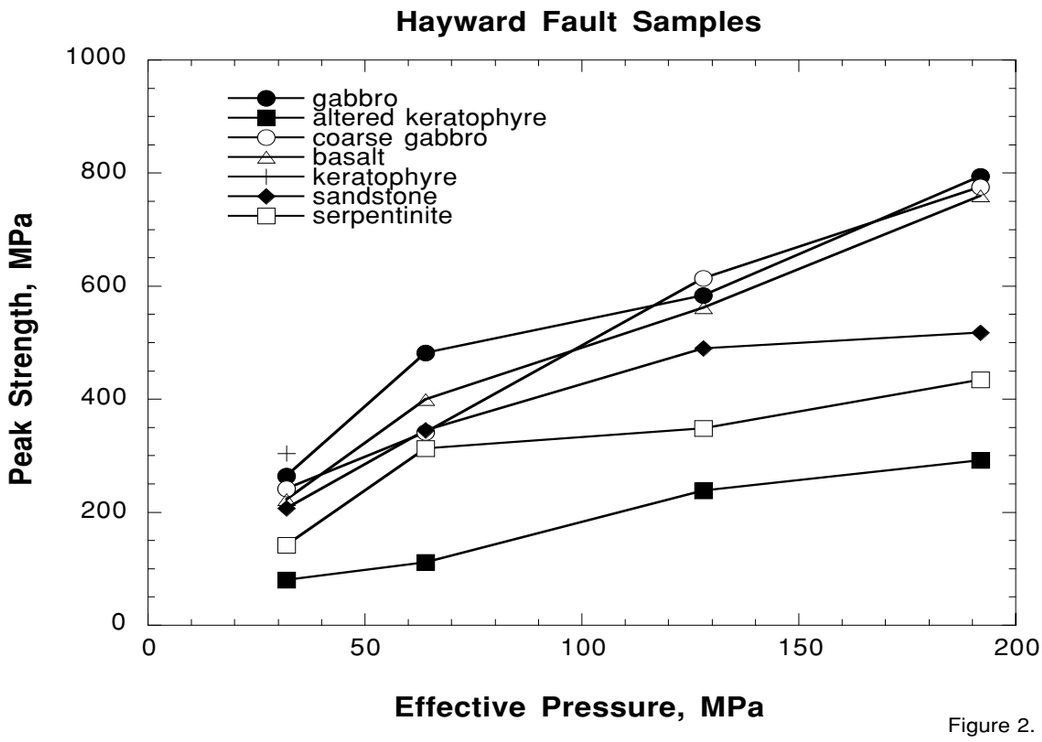

Figure 2.

Figure 2. Peak strength versus effective pressure.

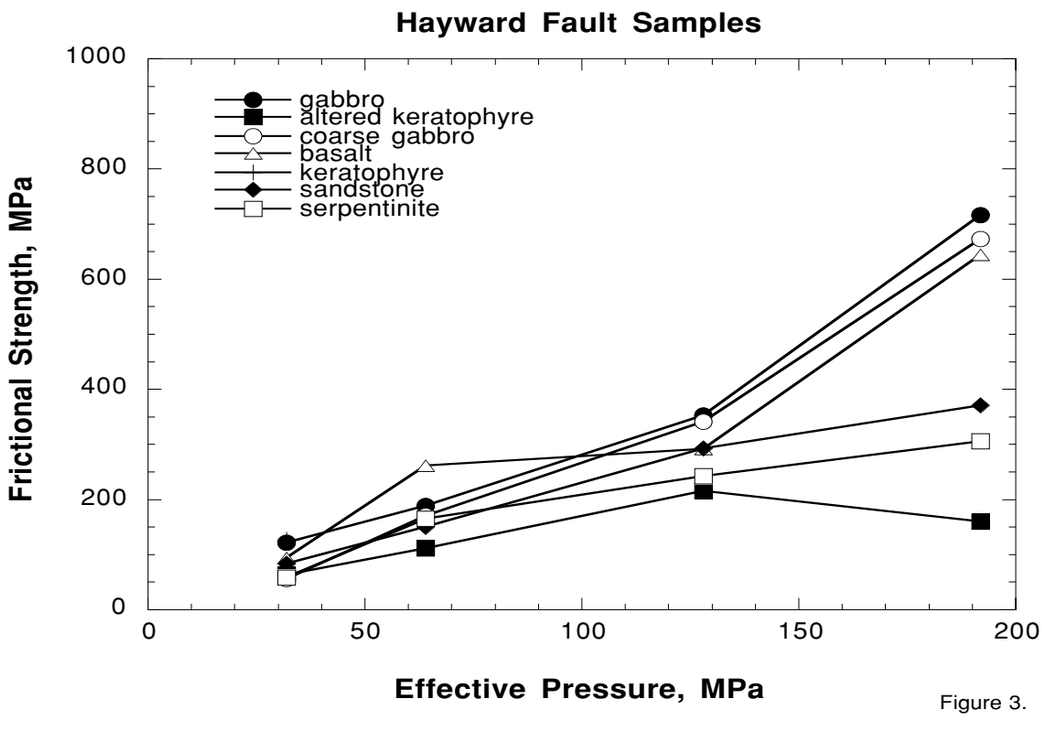

Figure 3.

Figure 3. Frictional strength (at 8 mm) versus effective pressure.

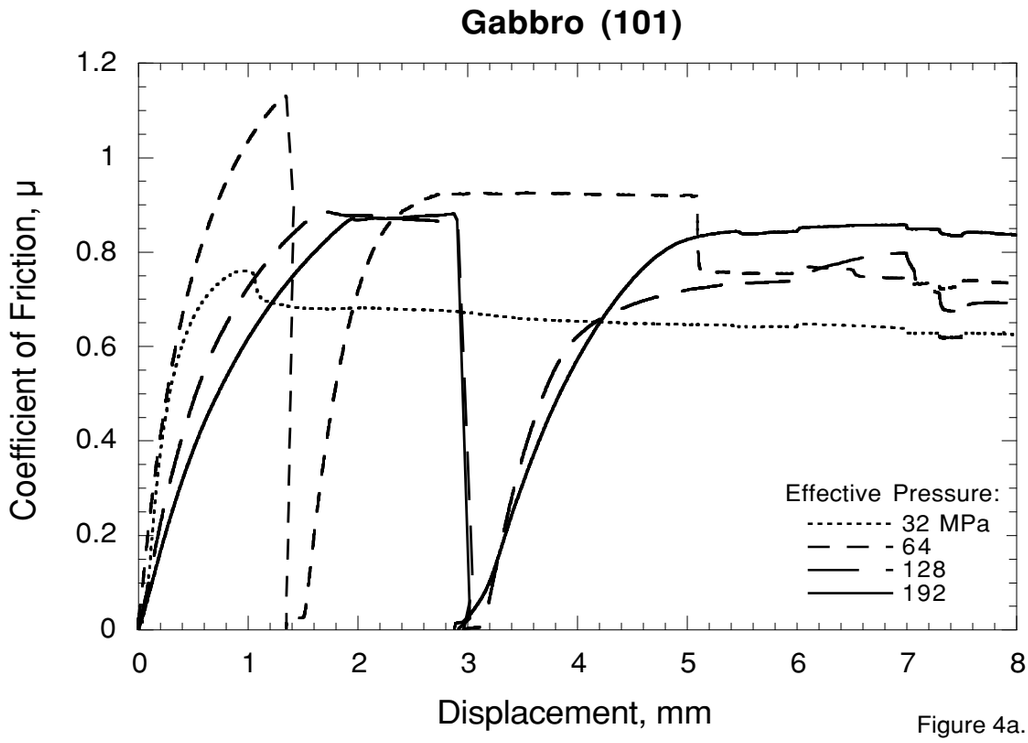

Figure 4a.

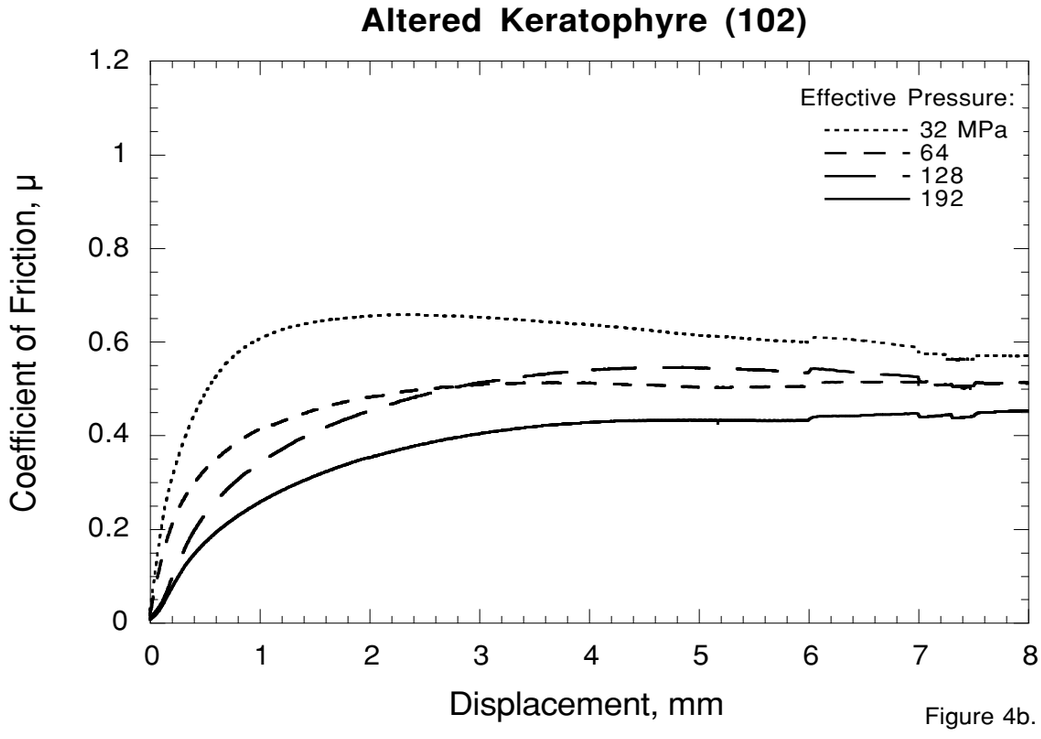

Figure 4b.

Figure 4. Coefficient of friction versus axial displacement at effective pressures of 32, 64, 128, and 192 MPa. a., Gabbro (101); b., Altered Keratophyre (102); c., Coarse Gabbro (103); d., Basalt (107); e., Keratophyre (111); f., Sandstone (114); and g., Serpentine (New Idria).

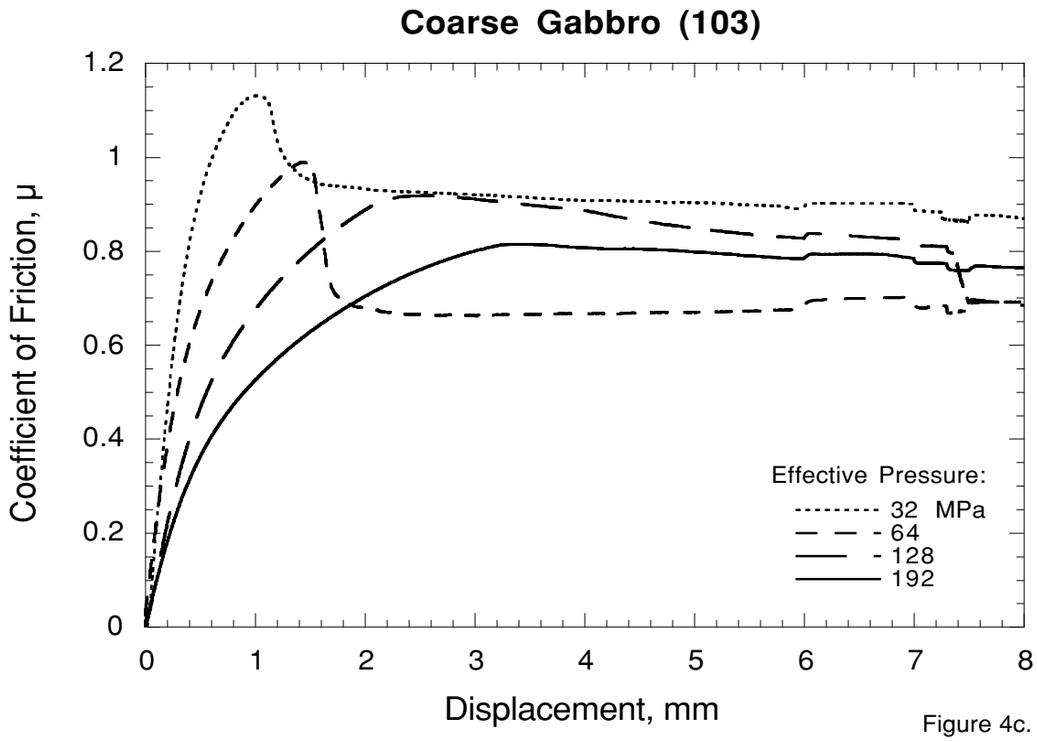

Figure 4c.

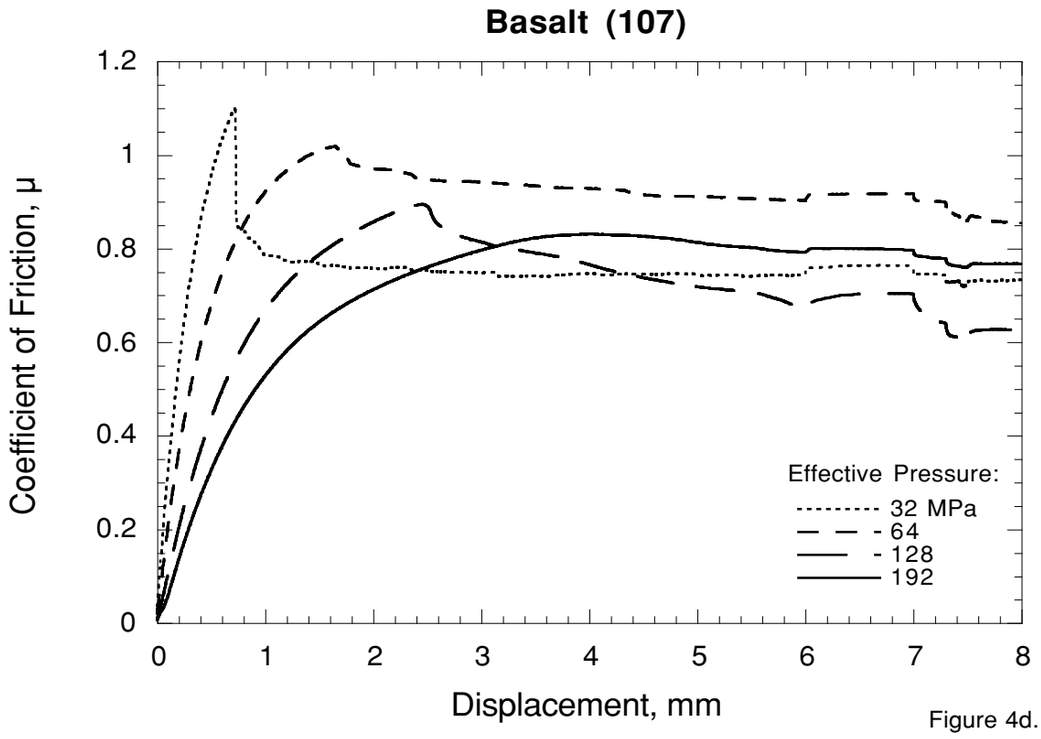

Figure 4d.

Figure 4. Coefficient of friction versus axial displacement at effective pressures of 32, 64, 128, and 192 MPa. a., Gabbro (101); b., Altered Keratophyre (102); c., Coarse Gabbro (103); d., Basalt (107); e., Keratophyre (111); f., Sandstone (114); and g., Serpentine (New Idria).

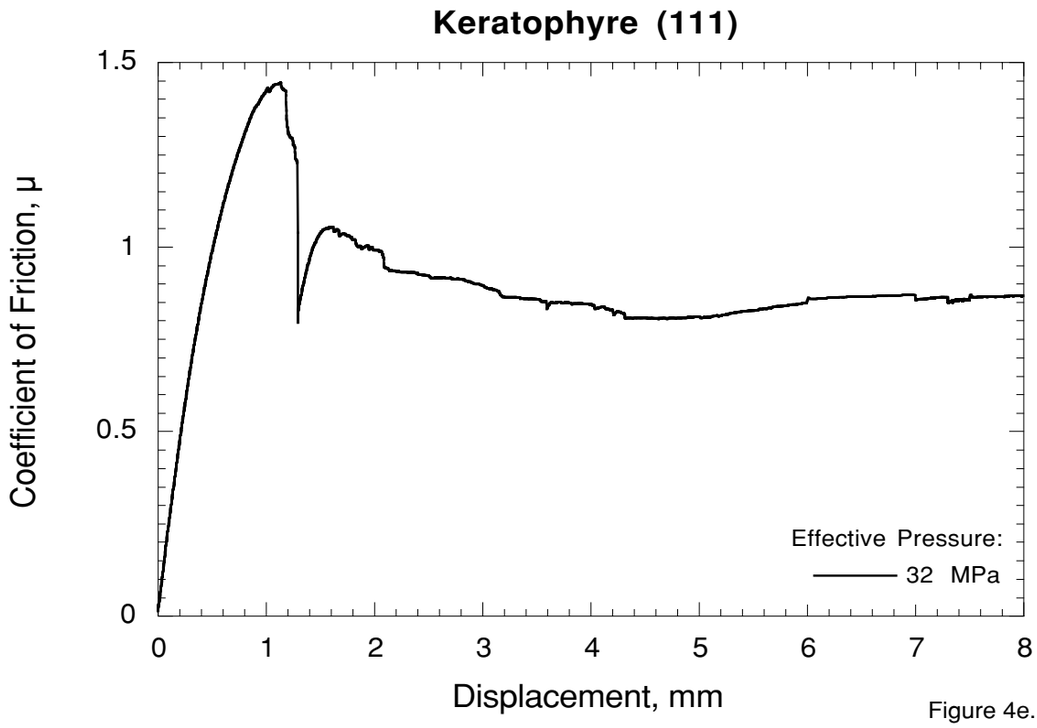

Figure 4e.

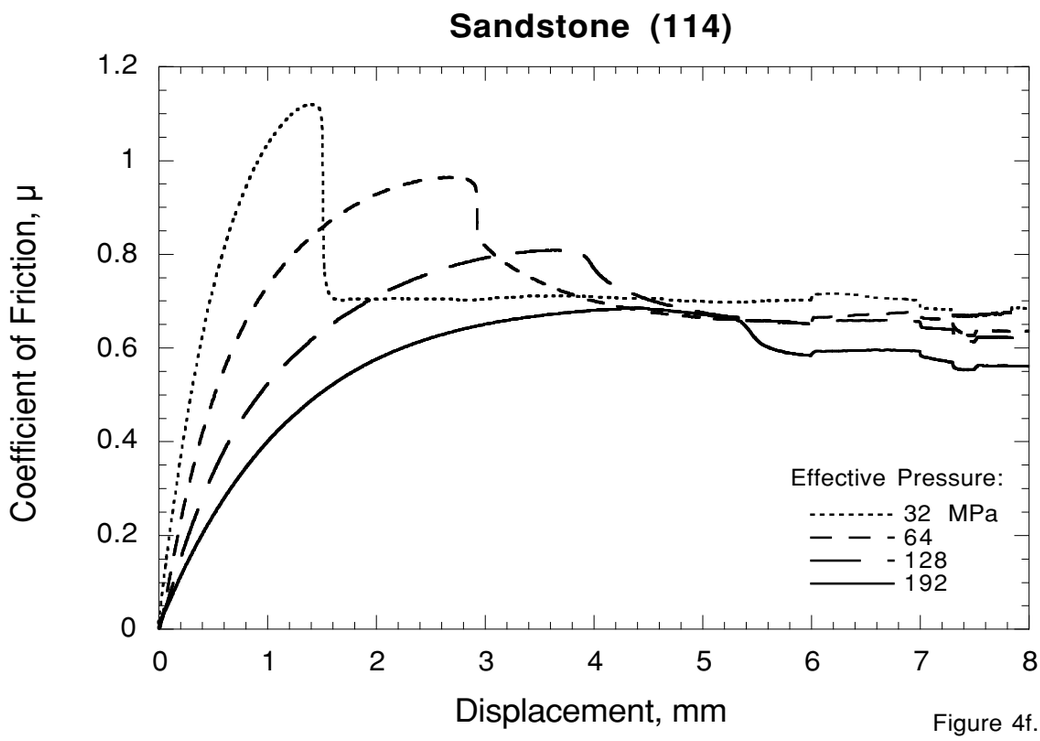

Figure 4f.

Figure 4. Coefficient of friction versus axial displacement at effective pressures of 32, 64, 128, and 192 MPa. a., Gabbro (101); b., Altered Keratophyre (102); c., Coarse Gabbro (103); d., Basalt (107); e., Keratophyre (111); f., Sandstone (114); and g., Serpentine (New Idria).

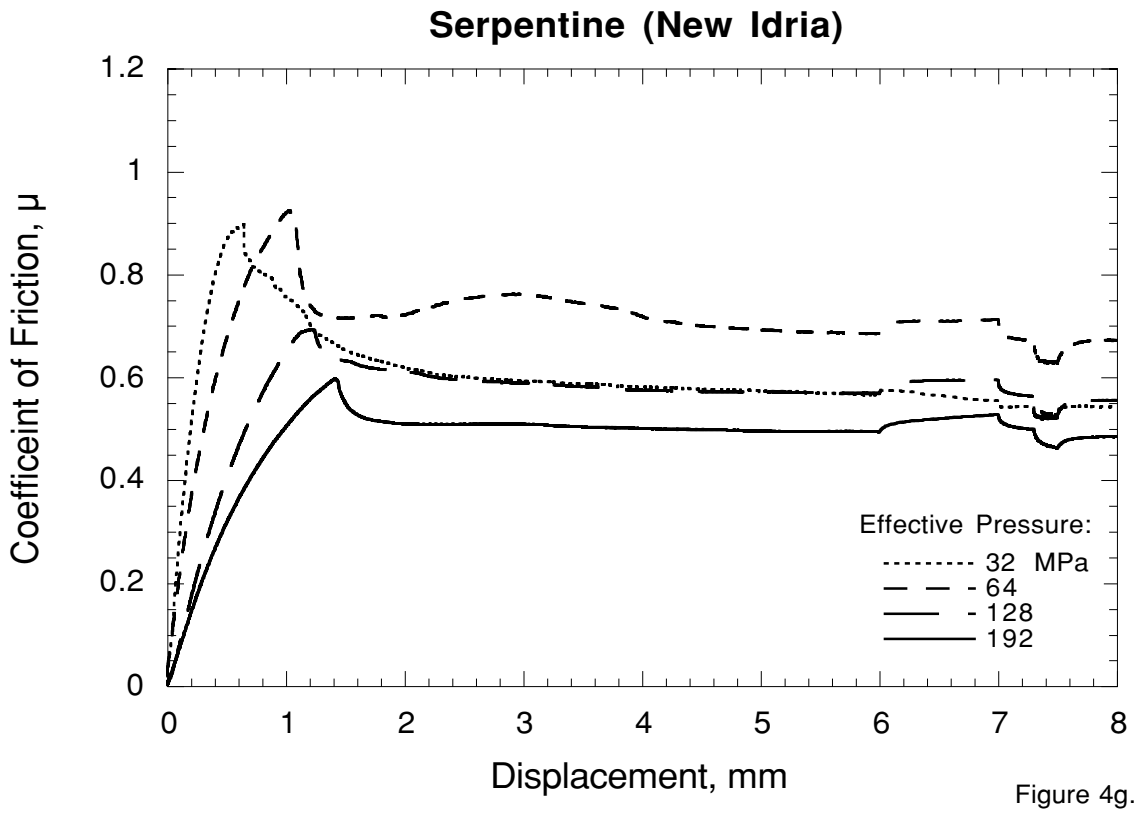

Figure 4. Coefficient of friction versus axial displacement at effective pressures of 32, 64, 128, and 192 MPa. a., Gabbro (101); b., Altered Keratophyre (102); c., Coarse Gabbro (103); d., Basalt (107); e., Keratophyre (111); f., Sandstone (114); and g., Serpentine (New Idria).

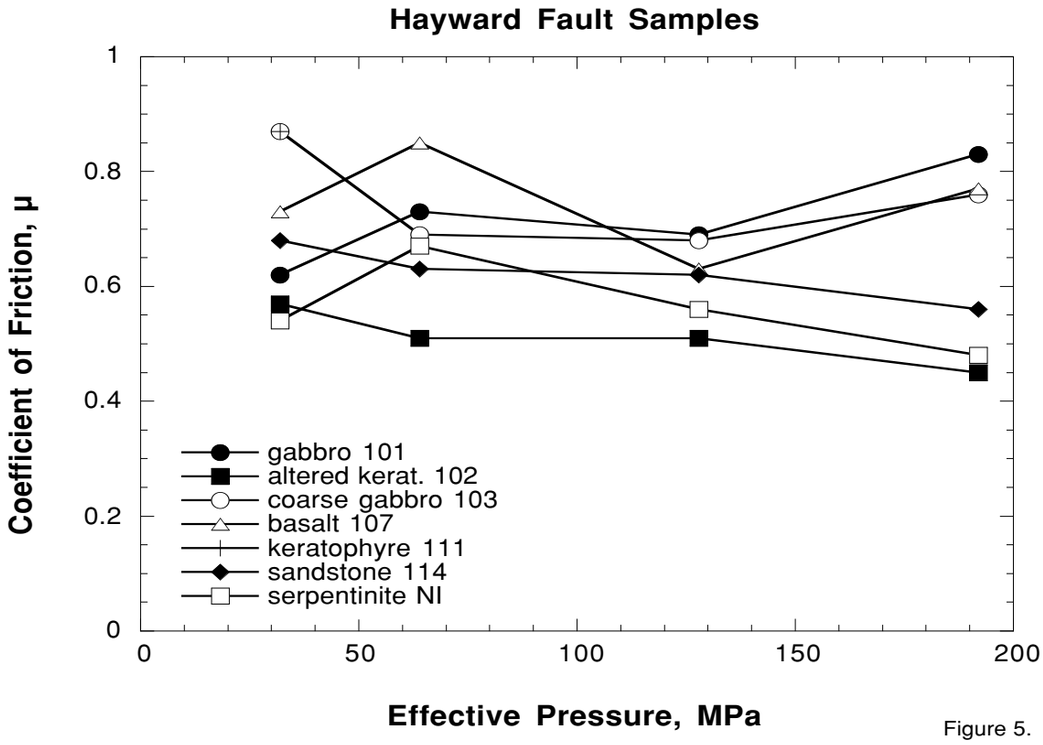

Figure 5.

Figure 5. Summary of coefficients of friction at 8 mm sliding.

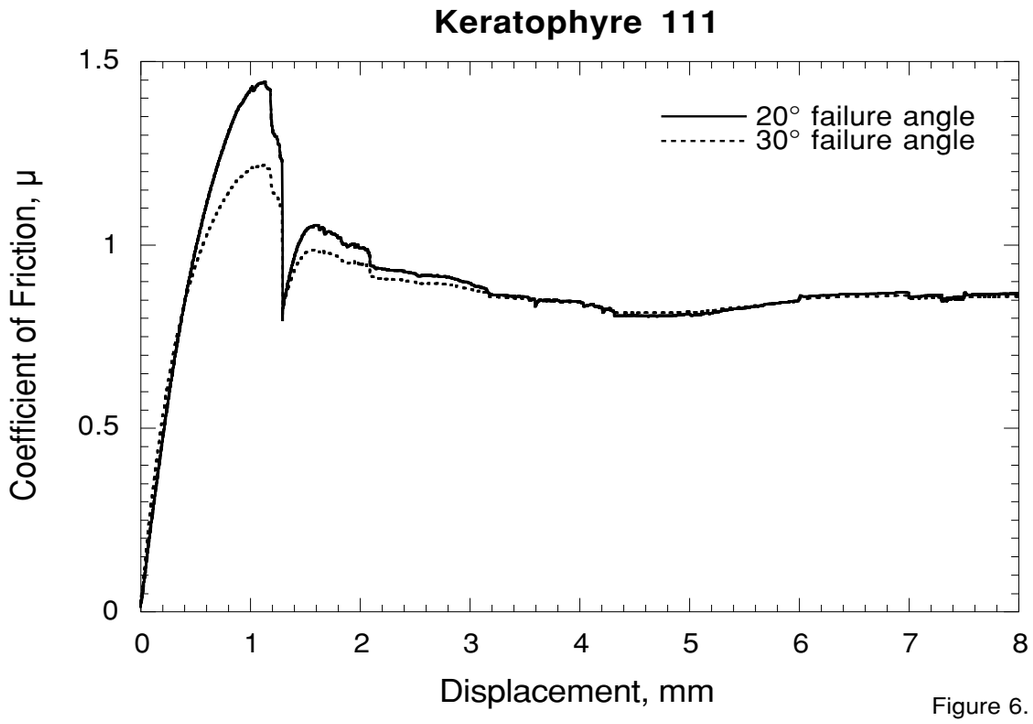

Figure 6.

Figure 6. Comparison of the coefficient of friction versus displacement of the keratophyre (111) with the observed failure angle of 20° and a reference failure angle of 30°.

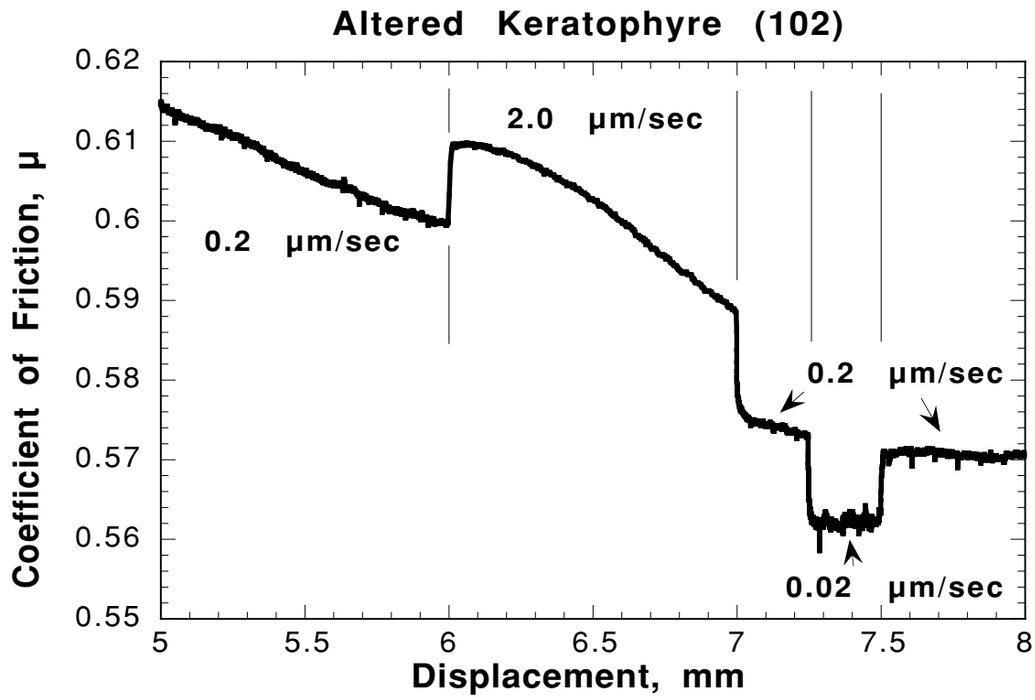

Figure 7.

Figure 7. Blowup of the coefficient of friction versus displacement during the velocity steps for the altered keratophyre (102).

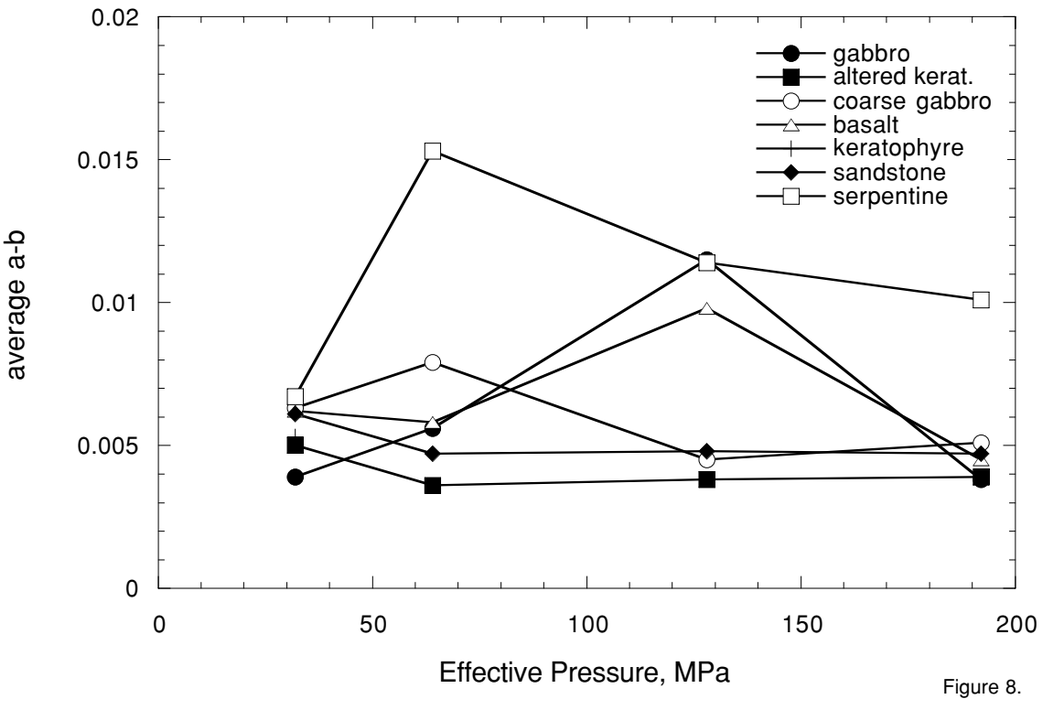

Figure 8.

Figure 8. Velocity dependence (a-b) versus effective pressure. All a-b values are positive.